Nanoscale Advances

ROYAL SOCIETY OF CHEMISTRY

PAPER

View Article Online
View Journal | View Issue

Cite this: *Nanoscale Adv.*, 2025, **7**, 8161

Edge and defect effects on charge distribution in collapsed MoS_2 nanotubes

Matjaž Malok, *[ab] Janez Jelenc, [a] Anja Pogačnik Krajnc [ab] and Maja Remškar [a]

Molybdenum disulfide (MoS_2) has emerged as a promising material for next-generation electronics and optoelectronic devices. MoS_2 nanotubes (NTs) and their collapsed ribbon-like shapes (collapsed NTs) synthesized *via* chemical vapour transport (CVT) under chemical equilibrium typically exhibit low structural defect densities. However, defects and surface damage can arise during device fabrication or operation, leading to a significant degradation in performance, stability, and operational lifetime. These imperfections also induce hysteresis, which adversely affects the device switching behaviour. While the influence of charge trapping at the MoS_2/substrate interfaces, on the MoS_2 surface, and at intrinsic defects, such as sulfur vacancies and dangling bonds, on device performance has been extensively studied, MoS_2 NTs, with their unique curved morphology, introduce additional charge-trapping mechanisms not observed in planar MoS_2 structures. In this work, a combination of scanning tunnelling microscopy (STM), Kelvin probe force microscopy (KPFM), and conductive atomic force microscopy (c-AFM) was employed to examine how structural irregularities, including terminated layers, surface-grown flakes or NTs, and highly strained areas, affect charge injection, redistribution, and the resulting effects on electrical characteristics in collapsed NTs. The results reveal that structural defects act as charge traps, scattering centres, and transport barriers, giving rise to a reduced carrier mobility, localized charge accumulation, and spatially inhomogeneous charge distribution. These findings underscore the crucial role of structural and electrical characterization with nanoscale resolution in the design of defect-tolerant, high-performance devices based on transition metal dichalcogenides (TMDs).

Received 12th August 2025
Accepted 1st November 2025

DOI: 10.1039/d5na00771b

rsc.li/nanoscale-advances

Introduction

The demand for next-generation electronics continues to drive research into advanced materials. Molybdenum disulphide (MoS_2), a layered transition metal dichalcogenide (TMD), has attracted significant attention due to its unique electronic and quantum properties in two-dimensional (2D) form.[1] Each MoS_2 monolayer consists of a molybdenum atomic plane sandwiched between two sulphur planes, forming a molecular layer 0.65 nm thick.[2] Atoms within a molecular layers are held together by strong covalent bonds, whereas adjacent layers are coupled by weak van der Waals (vdW) interactions.

MoS_2 exhibits diverse morphologies, including hollow and collapsed nanotubes (NTs).[3] Among various synthesis methods,[4] chemical vapour transport (CVT) under near-thermodynamic equilibrium condition produces high-quality crystalline structures.[5] Collapsed NTs form during growth, adopting a ribbon-like morphology with rounded edges and a chiral 2Hb stacking sequence.[6] The degree of structural collapse varies from slightly deformed tubes, which retain a small interlayer gap[6] to fully collapsed NTs resembling a single-crystal structure.[7] At edges of the collapsed NTs, the molecular layers are partially split, but despite a significant bending, they remain intact[7–9] and form rounded edge shapes.

Electronic structure calculations based on density-functional tight-binding (DFTB) theory indicates that MoS_2 NTs remain semiconducting regardless of diameter.[10] The zigzag NTs typically exhibit a small direct bandgap, whereas the armchair NTs may display either direct or indirect gaps depending on their chirality. The bandgap is dependent on geometry and is generally smaller than that of bulk MoS_2. A tensile strain further modifies the electronic structure, as the bandgap closes completely under 11% elongation, inducing a semiconductor-to-metal transition.[11]

MoS_2 demonstrates highly anisotropic conductivity due to its layered structure.[12] The in-plane conductivity exceeds the out-of-plane conductivity by more than three orders of magnitude.[13,14] Conductivity increases with decreasing flake thickness and varies with crystal orientation. In the zigzag direction, MoS_2 exhibits higher conductivity than in the armchair direction due to a wider band gap along the armchair direction and differences in depletion regions.[15] Interlayer rotation affects the out-of-plane transport, particularly for electrons, whose mobility

[a]*Solid State Physics Department, Jozef Stefan Institute, Ljubljana, Slovenia. E-mail: matjaz.malok@ijs.si*

[b]*Faculty of Mathematics and Physics, University of Ljubljana, Ljubljana, Slovenia*

decreases exponentially with increasing twist angle.[16] Transport measurements at cryogenic temperatures indicate a quantized conductance in MoS_2 NTs, suggesting transport through discrete quantum levels.[17]

Current flow in 2D devices is influenced by both vertical carrier distribution and resistance. While bottom-gate fields concentrate carriers near the substrate, surface n-doping (up to 10 000 times stronger than in the bulk) favours conduction near the surface.[14] This effect, combined with the high out-of-plane resistance and higher mobility in upper layers, results in a dominant current flow along the top layers.[12,18] Furthermore, the injected carriers can be segregated in thick MoS_2 samples due to layer-dependent Fermi-level pinning. In air-exposed MoS_2, electrons dominate the top layers, resulting in the n-doping at the surface, whereas holes reside in the inner layers, which remain weakly n-doped or intrinsic, minimizing the impact of the built-in potential barriers.[19]

CVT-grown MoS_2 NTs have demonstrated potential as electric field emitters[20] and as field-effect transistors (FETs).[9] These NTs can confine electromagnetic fields, supporting whispering gallery modes (WGM),[21] which evolve with changes in the NT's cross-section.[22] Additionally, they exhibit intrinsic piezoelectricity, enabling direct coupling between mechanical deformation and electronic response.[23]

Despite this potential, the device performance is challenged not only by inherent contact limitations,[24,25] but also by pervasive charge trapping. This phenomenon is a dominant factor in device degradation, significantly impairing performance, stability, reliability, and lifespan, while it also induces a performance-altering hysteresis.[26,27]

In this study, scanning tunnelling microscopy (STM), Kelvin probe force microscopy (KPFM), and conductive atomic force microscopy (c-AFM) are employed to investigate how surface defects, such as terminated layers, surface-grown structures, and highly strained edges, influence a charge spreading across collapsed NTs, and to understand the subsequent implications for the MoS_2-based electronic device performance.

Experimental

Synthesis

MoS_2 was synthesised *via* a chemical vapour transport (CVT) reaction at 1010 K within a sealed quartz ampoule, using iodine as the transport agent. The predominant product consisted of thin, highly corrugated MoS_2 sheets. During the final stages of growth, MoS_2 NTs nucleated on the surfaces of these flakes. A subset of the NTs underwent structural collapse upon encountering physical barriers, which induced mechanical strain and brought the opposing walls into close proximity. Subsequent vdW interaction promoted the walls to coalesce, yielding the flattened, ribbon-like structures and resulting in structurally stable collapsed NTs.[3] The structural properties of these NTs have been characterized previously using scanning electron microscopy (SEM), transmission electron microscopy (TEM), and Raman spectroscopy.[7]

Sample preparation

The collapsed NTs (15–30 nm thick and 1–3 μm wide) were transferred onto a p-doped silicon substrate (Siegert Wafer), as shown in Fig. 1a, using an adhesive tape method (Nitto Denko ELP BT-150E-CM). The silicon substrate served as a grounded bottom electrode for all measurements. For electrical characterization, an AFM tip was positioned above an individual collapsed NT, acting as a movable top electrode. This configuration enabled a localized charge injection and subsequent measurement of the NT's electrical response, as schematically illustrated in Fig. 1b.

Probe microscopy

Atomic force microscopy (AFM), Kelvin probe force microscopy (KPFM), and scanning tunnelling microscopy (STM) measurements were performed using a VT-AFM system (Scienta Omicron) under ultra-high vacuum conditions ($\sim 10^{-9}$ mbar). For KPFM, a modulation voltage was applied to the probe tip. A platinum-coated silicon tip (NSG30/Pt, NT-MDT, Spectrum Instruments) was used, featuring a nominal tip radius of 35 nm, a resonance frequency of 320 kHz, and a force constant of 40 N m^{-1}.

Charge injection

Charge injection was performed in STM mode on the top surface of collapsed MoS_2 NTs. Prior to injection, individual collapsed NTs were identified using non-contact AFM, and baseline contact potential difference (CPD) values were recorded relative to the silicon substrate. The system was then

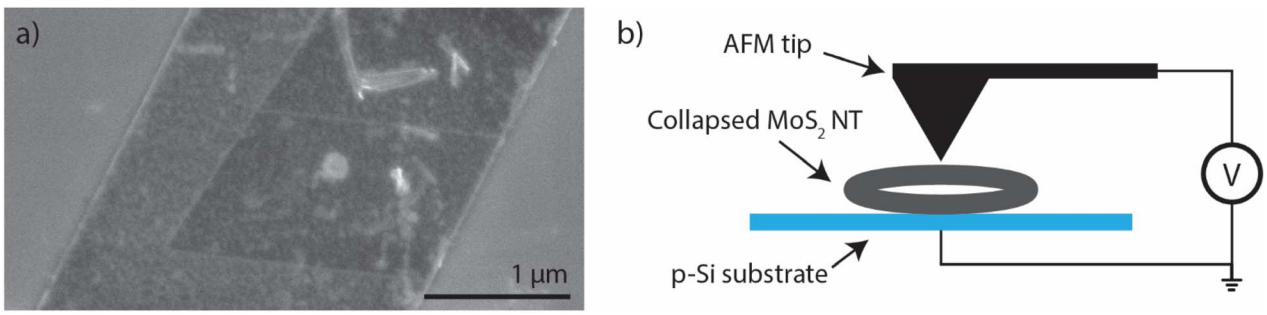

Fig. 1 (a) SEM image of the collapsed MoS_2 NT on a p-Si substrate. (b) Schematic diagram of the experimental setup: the MoS_2 NT is put on the grounded p-Si substrate, while the AFM tip serves as a movable top electrode, enabling localized charge injection and subsequent measurement of the NT's electrical properties.

switched to STM mode, where voltage biases ranging from −8 V to +8 V were applied to the probe tip. A steady tunnelling current of 333 nA was maintained for 6 minutes at each selected bias, ensuring a consistent total injected charge. Continuous current monitoring verified the integrity of the electrical contact throughout the process. Injection of electrons occurred under negative bias, whereas positive bias facilitated injection of holes into the collapsed NT. After each injection step, the system was switched back to the KPFM mode to measure CPD changes induced by charge injection and its redistribution. CPD profiles were referenced to the silicon substrate. Topographic data were levelled using the Max Flatness Tilt function in SPIP 6.7.5 software (Image Metrology). To correlate structural and electronic modifications, line scans of both surface topography and CPD were extracted from the same regions on the NTs before and after each charge injection.

Results

Terminated layers and structures on the surface

First, we examined how the terminated MoS_2 layers and other surface features influence charge spreading and its distribution across the collapsed NT. Fig. 2a presents a nc-AFM image of the collapsed NT with a visible distinct rhomboidal region, which is resolved also in Fig. 1a. Two line profiles (Fig. 2b) taken in parallel with the left (blue) and bottom (green) edges of the region, reveal a step-like height variation of approximately 0.6 nm, indicating that the rhomboid protrudes roughly 0.6 nm above the surrounding collapsed NT surface. This height difference corresponds to one additional molecular layer above the area left and below the rhomboid. The surface above the rhomboidal region is approx. 1 nm higher, suggesting that the rhomboidal structure comprises two layers less than the area

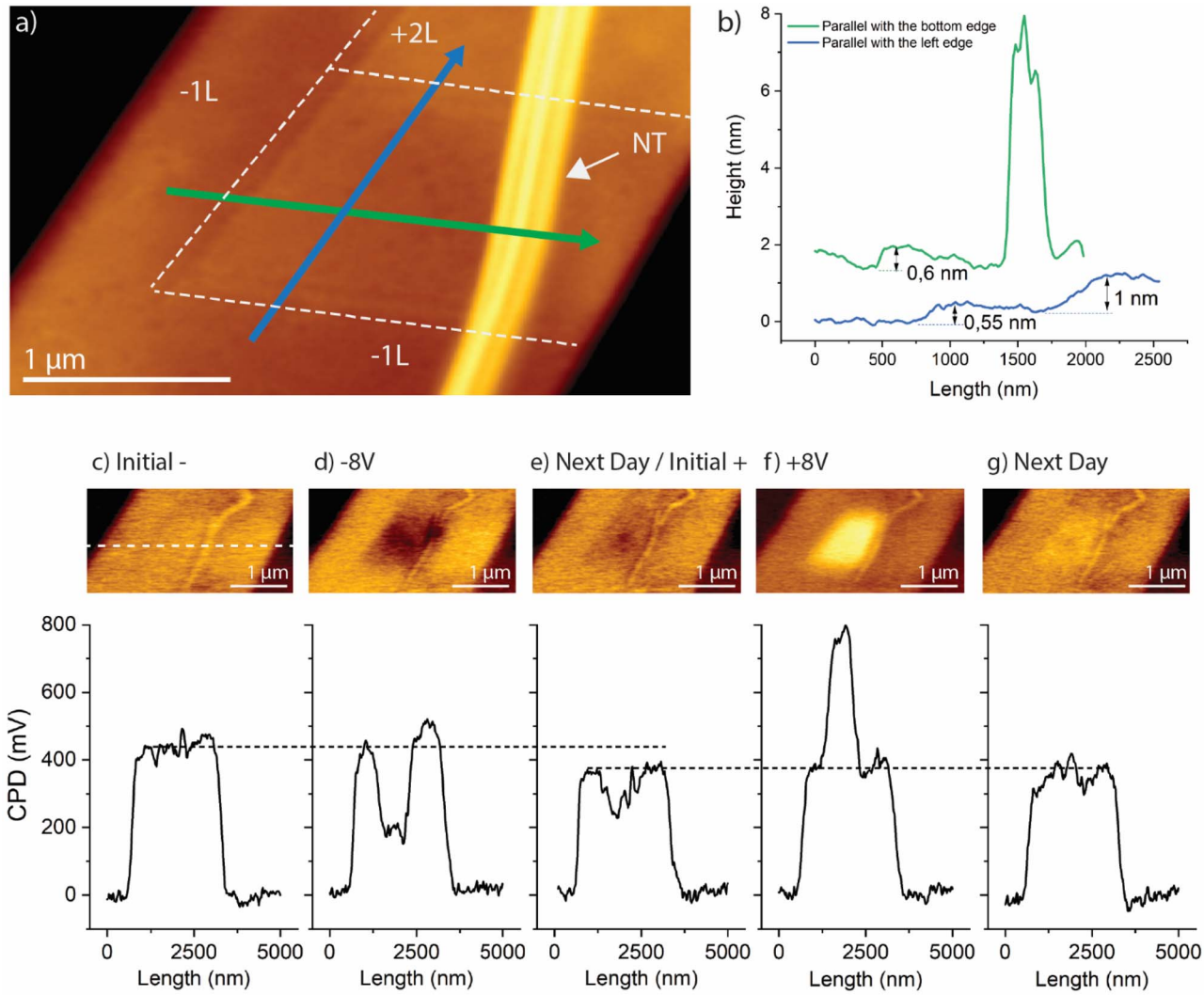

Fig. 2 Effect of charge injection into a rhomboidal flake located on the surface of a collapsed NT. (a) Topographical image of the flake, bounded on the left, top, and bottom by a terminated MoS_2 layer (white dashed lines), and on the right by an NT lying on the surface. (b) Cross-sectional profiles taken in parallel with the left (blue) and bottom (green) termination of the rhomboidal region, corresponding to panel (a). (c)–(g) KPFM images (top) acquired across the collapsed NT, as indicated in panel (a): (c) before charge injection; (d) immediately after injection of electron at −8 V; (e) 24 hours after injection of electron at −8 V; (f) immediately after hole injection at +8 V; (g) 24 hours after hole injection at +8 V.

above it. These observations confirm the presence of locally terminated MoS_2 layers, which are expected to significantly influence charge accumulation and its transport within the collapsed NT. In addition, a MoS_2 NT, 6 nm in height, was lying across the rhomboidal region on the collapsed NT surface. The rhomboidal region was confined all around.

Fig. 2c shows the initial state before charge injection. First, electrons were injected into the rhomboidal region. As shown in Fig. 2d, the CPD decreased from the initial 420 mV to 190 mV, but this change was confined to the rhomboidal region. Charge spreading was limited by the terminated MoS_2 edges on the left, bottom, and top, as well as by the NT present on the surface. In 24 h (Fig. 2e), the CPD of the rhomboidal region increased to 350 mV, while the CPD of the surrounding NT area decreased to 380 mV. Then, holes were injected into the rhomboidal region. As shown in Fig. 2f, the CPD of the rhomboidal flake increased from 370 mV to 800 mV. In the next 24 h (Fig. 2g), the CPD of both the rhomboidal region and surrounding areas returned to their pre-injection value (around 420 mV). These results demonstrate that the terminated layers, as well as surface-grown structures such as collapsed NTs, effectively restrict a rapid charge spreading across the surface.

To verify that the NT situated on the collapsed NT surface restricted charge spreading, the charge injection experiment was repeated after the NT was inadvertently removed (SI Fig. S1) from the rhomboidal region by the AFM tip. Although the NT was largely removed, some remnants remained on the surface, affecting subsequent scanning. Fig. 3 presents CPD profiles of the same area recorded before (bright lines) and after (dark lines) injection of electrons at −8 V bias, with green lines corresponding to the case when the NT was still present, and red lines after its removal (SI Fig. S2). When the NT was in place, the injected charge did not propagate beyond it, indicating that the

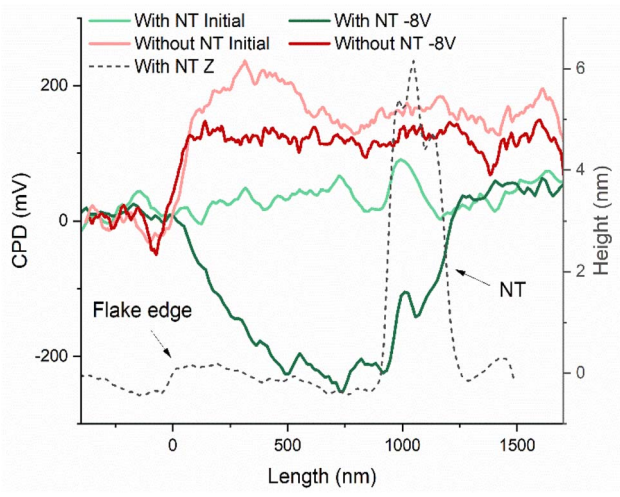

Fig. 3 Influence of the NT on charge spreading. Red lines represent measurements with the NT present on the surface, while green lines correspond to measurements after the NT removal. Bright lines represent the pre-injection state, and dark lines indicates post-injection state. The dashed line indicates the topography of the scanning area when the NT was still on the surface.

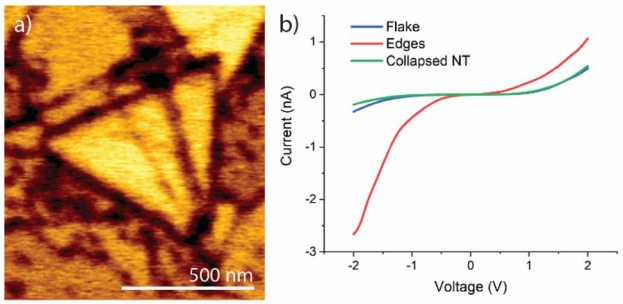

Fig. 4 (a) KPFM image of the flake separated from the surrounding area, showing a lower WF at its edges. (b) Conductivity measured on the flake surface (blue), at the flake edges (red), and on the surrounding collapsed NT surface (green).

NT acted as a physical barrier to charge distribution. After the NT was removed, the charge spread into the area previously occupied by the NT (Fig. 3, red). However, the CPD change right from the former NT location was less pronounced than on the left side. This reduced CPD change is likely due to residual fragments of the NT, which continued to partially obstruct charge transport across the surface.

In contrast to the previously described rhomboidal flake, which remained connected to the bulk at its bottom and at the upper side, Fig. 4a shows a triangular and folded flake (2 nm thick), which was completely separated from the side surface of a collapsed NT on which it was laying. The KPFM image (Fig. 4a) reveals that the work function (WF) at the edges of the flake was lower than that of its central surface. Both edges of the fold, upper (A) and lower (B) one, are also resolved as dark lines corresponding to decreased WF. Fig. 4b presents the extracted *I–V* spectra from the flake's surface, its edges, and the underlying collapsed MoS_2 NT surface. The *I–V* spectra indicate that the edges of the flake exhibited a higher conductivity than both the flake surface and the collapsed NT surface. While the surfaces displayed n-type behaviour, the edges exhibited p-type behaviour.

Strained structures

Charge was injected into the central part of a folded region of a collapsed NT (18.3 nm thick and 1 μm wide), as shown in SI Fig. S3. The KPFM images and corresponding cross-sectional CPD profiles acquired across the fold (red), below it (blue) and above it (green) reveal distinct potential modulation. Injection of electrons resulted in a decrease in the CPD of the folded region (Fig. 5b), whereas injection of holes increased the CPD of this region (Fig. 5d). The CPD values of the surrounding collapsed NT surface, however, remained unchanged, indicating that the injected charges were confined in the folded area.

In 24 h after injection of electrons, the CPD of the folded region (Fig. 5c) exhibited only partially recovered towards its original level, in contrast to the nearly complete recovery observed after injection of holes (Fig. 5e). Notably, no significant change in CPD was detected on the adjacent regions until

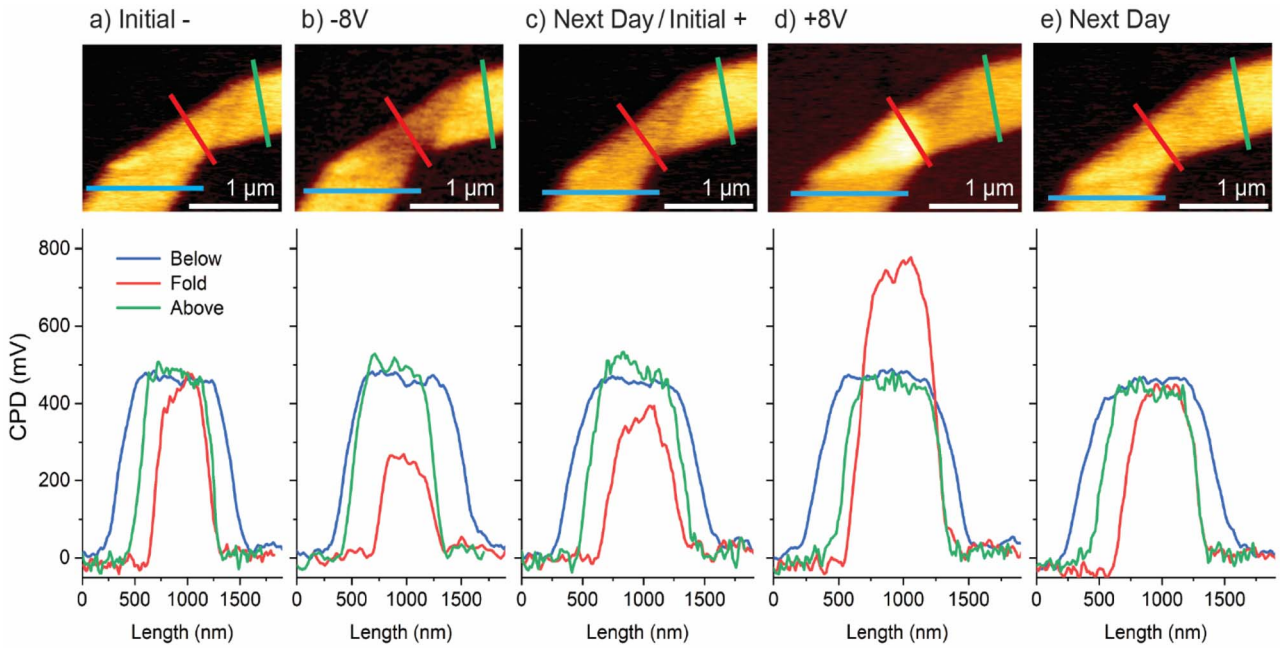

Fig. 5 KPFM images of the folded collapsed MoS_2 NT (top) with the corresponding line profiles (bottom). Line profiles were extracted below the fold (blue), on the fold (red) and above the fold (green): (a) before charge injections; (b) immediately after injection of electrons at −8 V; (c) 24 h after injection of electrons at −8 V; (d) immediately after injection of holes at +8 V; (e) 24 h after injection of holes at +8 V.

the following day. These observations suggest that the highly curved longitudinal edges of the collapsed NT, enclosing the folded segment, acted as an effective potential barrier that confined charge during and immediately after injection by suppressing the lateral charge diffusion.

Localized charge

Charge localization at the injection spots was observed during charge injection experiments at the terminal end of the same collapsed NT (SI Fig. S3). Fig. 6 shows KPFM images of the same location before injection (a), immediately after injection (b), and 24 h later (c). Electrons were injected at −2 V, −4 V, and −6 V at three nearby locations (Fig. 6b). Corresponding line profiles were extracted at the −2 V injection site (blue) and between the −2 V and −4 V injection spots (red). After all injections, the CPD at the injection spots decreased, appearing as dark spots in Fig. 6b. This reduced CPD remained highly localized in the injection spots, with no detectable changes observed in other regions of the collapsed NT surface. After 24 h, the CPD map revealed a uniform potential across the entire collapsed NT surface, with the injection spots no longer visible. However, the overall CPD remained lower (Fig. 6c) than the initial, pre-injection value (Fig. 6a). This temporal evolution suggests that the injected charges, while initially localized at the injection sites, gradually redistributed uniformly across the collapsed NT surface.

Electronic effect of charge injection

Changes of the *I–V* characteristics caused by charge injections were investigated on a collapsed NT, 1.2 μm wide and 15.6 nm thick, using scanning tunnelling spectroscopy (STS). Spectroscopy measurements were performed before injections, and started immediately after injections. The following injection was performed around 45 min after the previous one.

After injection of holes at +8 V, the *I–V* spectrum at negative voltages did not change, but at positive voltages it was suppressed with regard to the spectrum before the injection. This means that conductance of holes was slightly reduced. After injection of electron at −8 V, the conductance of electrons was slightly reduced, but conductance of holes was strongly enhanced. The *I–V* characteristics were virtually shifted towards right due to injection of holes and towards left due to injection of electrons.

Discussion

The distribution and dynamics of injected charge across various structural features on collapsed MoS_2 NT surfaces, including surface steps with exposed terminated layers, highly strained edges, and surface-grown nanostructures such as secondary grown NTs, were investigated through point charge injections in STM mode. In this configuration, the tip acted as the injecting electrode, while the p-type silicon substrate beneath the collapsed NT served as the grounded electrode (Fig. 1b). Upon injection, the charge dispersed laterally from the injection site, driven primarily by Coulomb repulsion and local potential variations.

MoS_2, like many other layered materials, exhibits a strong electrical anisotropy, as its in-plane conductivity ($\sigma_{\parallel}$) exceeds the out-of-plane conductivity ($\sigma_{\perp}$) by more than three orders of magnitude.[12,14] This anisotropy strongly favours in-plane

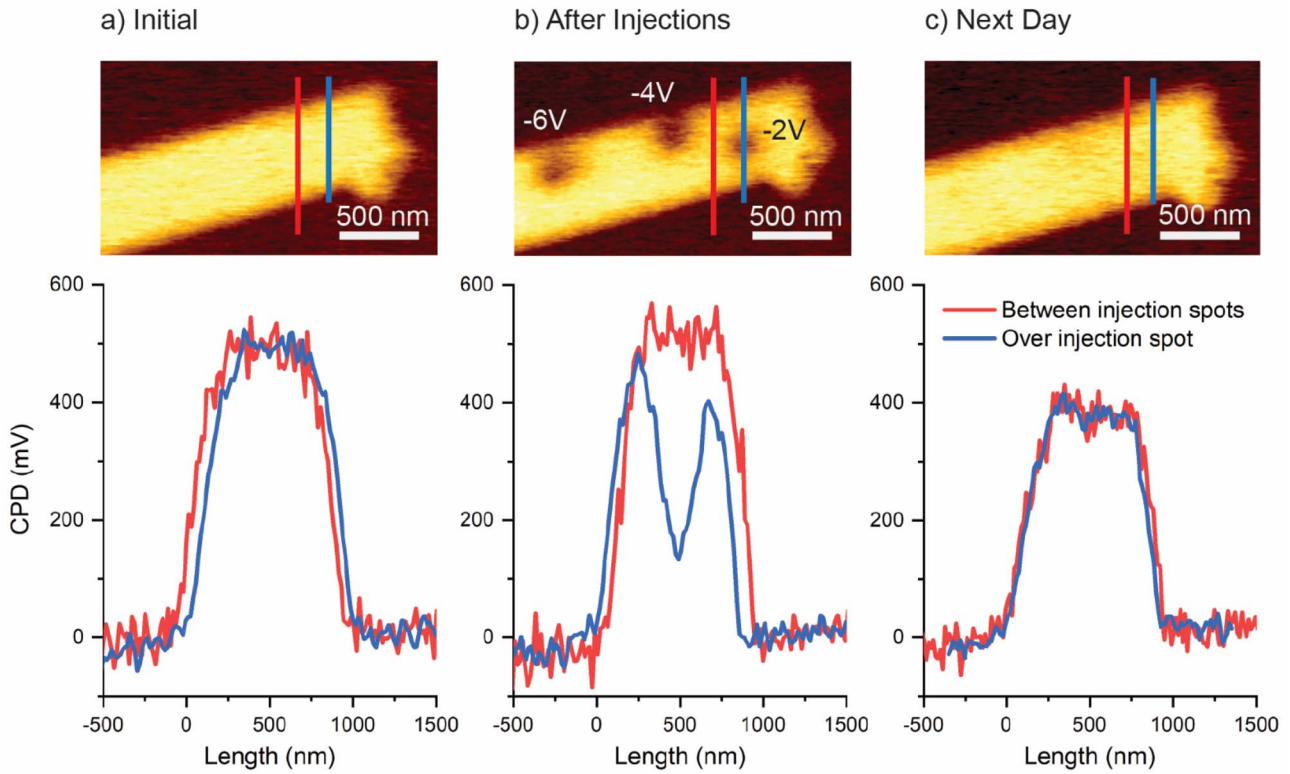

Fig. 6 KPFM images (top) and corresponding line profiles (bottom) acquired between injection spots (red) and across an injection spot (blue). (a) Initial state before charge injection; (b) immediately after charge injections at −2 V, −4 V, and −6 V, showing well-defined localized injection spots; (c) 24 h after injections, revealing partial charge recombination and redistribution across the collapsed MoS_2 NT surface.

current flow over the vertical transport across the vdW-stacked layers. Considering charge injection at the centre of a 3 μm wide and 17 nm thick NT (Fig. 1a), the ratio of perpendicular to lateral current can be estimated:

$$\frac{i_\perp}{i_\parallel} = \frac{R_\parallel}{R_\perp} = \frac{\rho_\parallel \cdot l_\parallel}{\rho_\perp \cdot l_\perp} = \frac{0.3\ \Omega\ \text{cm} \times 1517\ \text{nm}}{30\ \Omega\ \text{cm} \times 17\ \text{nm}} \approx \frac{1}{1}$$

where i denotes the electrical current in the in-plane (∥) and out-of-plane (⊥) directions, R is the resistance, ρ the resistivity[28] and l is the effective current path length in the in-plane (1517 nm) and out-of-plane (17 nm) directions. This relation indicates that approximately the same amount of charge is expected to flow laterally (in-plane) toward the substrate *via* the NT edge than vertically through the vdW-stacked layers, despite the shorter vertical distance to the substrate.

However, the experiments have shown that the injected charge accumulates predominantly on the NT surface rather than being transferred efficiently into the underlying silicon substrate. This behaviour can be attributed to the structural imperfections such as defects, dangling bonds, or adsorbates that act as charge traps;[14] the presence of a Schottky barrier at the MoS_2–Si interface that impedes charge transfer;[29–31] and local structural defects, including terminated layers and highly strained regions, that can confine charge transport laterally. Collectively, these factors form potential barriers that govern both the charge distribution and current pathways within the collapsed NT.

Fig. 2 demonstrates how terminated layers of surface-grown flakes can hinder charge spreading. Edge states strongly influence carrier transport, as MoS_2 zigzag edges exhibit vanishing band gaps with metallic states running parallel to the edges, whereas armchair edges retain semiconducting behavior,[32–34] Passivation of the dangling bonds further modifies these electronic properties.[35,36] As a result, edges can form natural p–n junctions, with p-doped edge states (originating from the dangling bonds) contrasting with the n-doped basal plane,[37,38] which potentially restrict the charge transfer across the edges. Initially, the injected charge remains confined within the top MoS_2 layer due to a weak interlayer coupling and electrostatic self-screening, which create a potential barrier for the interlayer transfer. However, as shown in Fig. 2, initially localized charge eventually redistributes across the entire collapsed NT surface. This redistribution may occur *via* charge hopping though defects or impurities,[39] a slow quantum tunnelling across energy barriers, or diffusion driven by local electric fields.

Regarding the significant influence of edges on electronic transport, their properties were thoroughly characterized. Fig. 4a reveals that the CPD at edges is lower than in the surrounding basal plane, reflecting the modification of both the WF and the local density of states by highly charged edges.[32,40,41] The *I*–*V* spectra presented in Fig. 4b indicate that the flake edges exhibit higher conductivity than both the flake surface and the collapsed NT surface. This behaviour, consistent with previous findings,[32,33] arises because the terminated layers enable

electron transport between the STM tip and the flake to occur predominantly in-plane relative to the MoS_2 layers, whereas transport on the surfaces away from the edges is largely limited to out-of-plane conduction.

The presence of a MoS_2 NT atop the collapsed NT further influenced charge transport by hindering the lateral carrier spreading (Fig. 3), analogous with the behaviour observed in carbon NTs, which can trap charges and act as confining barriers.[42]

STS studies (Fig. 7) reveal charge-injection-induced modifications of the sample's local electrostatic potential. Injection of holes corresponding to a net electron removal, causes a suppression of the electronic density of states relative to the tip. This realignment enhances tunnelling at negative tip biases by providing more empty sample states for electrons from the tip, while simultaneously suppressing tunnelling at positive biases, as the occupied sample states are pushed to lower energies, thus requiring a higher tip voltage for electron extraction.

Conversely, negative charge injection, corresponding to net electron addition, induces an upward shift of the density of states. This new alignment suppresses electron injection at negative tip biases due to lack of empty states, resulting in a leftward shift of the *I–V* curve in this regime. At positive biases, tunnelling is strongly enhanced because the occupied sample states move closer to the tip's Fermi level, steepening the *I–V* slope and contributing to the overall leftward shift of the *I–V* characteristics.

When materials with different WFs come into contact, charge redistribution occurs until Fermi level alignment is achieved, producing local electric fields, band bending at the interface, and potential formation of electron depletion and accumulation regions, which can affect conductivity.[43] Additionally, the NT may introduce a local electrostatic gating effect doping the underlying collapsed NT and forming a conductivity bottleneck.[44] The formation of moiré patterns between MoS_2 nanoribbon and the MoS_2 sheet can induce lattice strain on the nanoribbon surface[45,46] modifying material electronic properties[47–52] and introducing periodic potential barriers that scatter charge carriers.

In the present configuration, with the MoS_2 NT atop the collapsed NT, CPD images (Fig. 2c) show comparable CPD values for the NT and the underlying collapsed NT. Since both electron and hole conductivities were confined, WF mismatch and the associated gating effect are unlikely to be the primary cause of reduced charge spreading. Instead, a more plausible explanation is the presence of imperfections at the vdW interface, such as voids, wrinkles, or trapped adsorbates, which act as scattering centres and limit carrier mobility. The persistence of CPD anomalies even after the NT was removed supports this interpretation.

When charge was injected into the folded region bounded by highly strained edges, lateral spreading was significantly restricted (Fig. 5). Although strain in MoS_2 is known to induce a semiconductor-to-metal transition by narrowing the bandgap and enhancing conductivity,[11] our CPD measurements showed no lateral charge flow beyond the bounded regions. This suggests the presence of additional energy states, likely caused by microcracks or other structural disruptions at the strained edges, that effectively terminate conductive pathways. Moreover, the intrinsic piezoelectric response previously demonstrated in collapsed MoS_2 NTs,[7] which could be introduced by charge injection and formation of potential gradient, may induce permanent changes in molecular configuration *via* plastic deformations. Such rearrangements can suppress hopping transport within the conduction channel or even trigger a metal-to-insulator transition.[53] These interpretations are supported by c-AFM measurements, which reveal increased conductivity at edges relative to flat regions, while also revealing localized zones of zero conductivity.[7] Interestingly, CPD values within the folded region partially returned to the initial values over time, whereas adjacent areas remained unchanged. This behaviour suggests that out-of-plane charge redistribution takes place preferentially through MoS_2 layers toward the substrate rather than laterally across structurally compromised edges.

The observed charge transport anomalies in collapsed MoS_2 NTs have significant implications for device performance and reliability.[53–56] It has been shown that charge trapping adversely affects electrical performance by degrading stability and reliability through reduced mobility, threshold voltage shift, and transient current decay,[27] while also dictating the switching behaviour *via* significant hysteresis dependent on the gate sweep history and through the induction of memory-like effects from floating gates.[26,57] Conversely, the same charge trapping mechanisms can be used for applications like analog synapses,[58] non-volatile memory and neuromorphic computing,[26,59,60] as well as multi-bit data storage.[61]

Charge trapping occurs at multiple physical sites, broadly categorized into interface, surface, and bulk defect-related sites. A substantial contribution originates from the interface between the MoS_2 channel and the gate dielectric.[27,57] For example, the SiO_2 surface possesses a high density of dangling bonds that create interface traps, causing strong dielectric

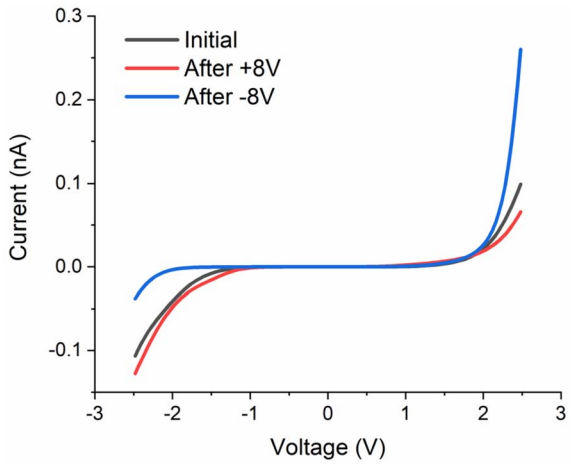

Fig. 7 STS measurements: *I–V* characteristics of a collapsed MoS_2 NT before charge injection (black), after injection of holes at +8 V (red), and after injection of electrons at −8 V (blue).

scattering.[27] Persistent hysteresis in suspended devices confirms that trapping is not solely a substrate effect,[62] but also the MoS_2 surface itself represents a major trapping site.[62] Ambient molecules such as H_2O and O_2 adsorb onto the surface, leading to water-assisted charge trapping.[26] Furthermore, fabrication residues like carbon contamination, can also act as trap states.[63] Intrinsic defects within the MoS_2 lattice, such as sulphur and oxygen vacancies, create localized states that trap charge.[26,63] Furthermore, extended structural defects, like pores, ripples, and nanobubbles formed during processing, contain dangling bonds or trapped ambient molecules, creating quasi-isolated regions that can store charge for extended periods.[59,61,64]

On the other hand, the geometry of MoS_2 NTs with rounded edges enables new charge trapping mechanisms. Strained edges can act as effective barriers to lateral charge transport, confining charge within top layers and approximating the behaviour of a planar MoS_2. Furthermore, terminated layers and other surface irregularities can impede or redirect current, resulting in a non-uniform charge distribution. Localized charge accumulation enhances electric field gradients, increases current density in confined regions and potentially accelerates device degradation. Such effects may form large electrostatic barriers that impair electrical transport,[65] underscoring the importance for comprehensive nanoscale electrical and structural characterization studies prior to a device integration to ensure predictable performance and reliability.

Conclusions

In this study, we investigated charge injection and its redistribution in collapsed MoS_2 NTs using a localized STM-based charge injection and KPFM as the characterization tool. Although MoS_2 NTs synthesized *via* CVT are believed to have a high structural perfection, their collapsed forms may exhibit distinct structural heterogeneities. Our findings reveal that the edges of terminated layers, detached surface flakes, highly strained regions, and surface adsorbates can significantly influence the charge transport. Despite the vertical proximity of the underlying silicon substrate, the injected charge preferentially propagated laterally due to a strong MoS_2's in-plane/out-of-plane electric conductivity anisotropy. However, this lateral spreading is often hindered by defects and topographical discontinuities such as terminated edges and interface imperfections. Regions exhibiting high strain and terminated edges effectively confine charge spread, as demonstrated by both c-AFM current mapping and CPD evolution over time. Additionally, overlying NTs and flakes altered local electronic properties through interfacial trapping, electrostatic gating, and strain-induced scattering. These findings underscore the importance of nanoscale structural integrity and interface quality in governing charge transport in 2D materials. They also highlight the necessity of a comprehensive nanoscale characterization prior to device fabrication to ensure predictable and reliable operation. Understanding and control of these localized charge dynamics will be essential for the design of reliable next-generation electronic and optoelectronic devices based on layered vdW materials.

Author contributions

M. M.: conceptualization, investigation, data curation, methodology, visualization, writing – original draft; J. J.: investigation, data curation, methodology; A. P. K.: SEM investigation; M. R.: funding acquisition, supervision, methodology, writing – review & editing.

Conflicts of interest

There are no conflicts to declare.

Data availability

The datasets are also available at **https://doi.org/10.5281/zenodo.17474142**.

All data supporting the findings of this study are provided in the main article and the supplementary information (SI). Supplementary information is available. See DOI: **https://doi.org/10.1039/d5na00771b**.

Acknowledgements

This research was supported by the Slovenian Research and Innovation Agency *via* grants P1-0099 and PR-11224.

Notes and references

1 O. Samy, S. Zeng, M. D. Birowosuto and A. El Moutaouakil, *Crystals*, 2021, **11**, 355.
2 X. Li and H. Zhu, *J. Mater.*, 2015, **1**, 33–44.
3 M. Remškar, Z. Škraba, F. Cléton, R. Sanjinés and F. Lévy, *Surf. Rev. Lett.*, 1998, **5**, 423–426.
4 U. Krishnan, M. Kaur, K. Singh, M. Kumar and A. Kumar, *Superlattices Microstruct.*, 2019, **128**, 274–297.
5 M. Remškar, *Adv. Mater.*, 2004, **16**, 1497–1504.
6 A. I. Galimov, *et al.*, *Nanoscale Horiz.*, 2024, **9**, 968–975.
7 M. Malok, J. Jelenc and M. Remškar, *Nanoscale*, 2025, **17**, 12361–12370.
8 M. Viršek, A. Jesih, I. Milošević, M. Damnjanović and M. Remškar, *Surf. Sci.*, 2007, **601**, 2868–2872.
9 S. Fathipour, *et al.*, *Appl. Phys. Lett.*, 2015, **106**, 022114.
10 G. Seifert, H. Terrones, M. Terrones, G. Jungnickel and T. Frauenheim, *PRL*, 2000, **85**, 146–149.
11 M. Ghorbani-Asl, S. Borini, A. Kuc and T. Heine, *Phys. Rev. B: Condens. Matter Mater. Phys.*, 2013, **87**, 235434.
12 W. Cao, M. Huang, C.-H. Yeh, K. Parto and K. Banerjee, *IEEE Trans. Electron Devices*, 2020, **67**, 1310–1316.
13 A. Souder and D. E. Brodie, *Can. J. Phys.*, 1971, **49**, 2565–2571.
14 M. D. Siao, *et al.*, *Nat. Commun.*, 2018, **9**, 1442.
15 F. Liu, Y. Wang, X. Liu, J. Wang and H. Guo, *IEEE Electron Device Lett.*, 2015, **36**, 1091–1093.

16 K. Zhou, D. Wickramaratne, S. Ge, S. Su, A. De and R. K. Lake, *Phys. Chem. Chem. Phys.*, 2017, **19**, 10406–10412.
17 R. T. K. Schock, J. Neuwald, W. Möckel, M. Kronseder, L. Pirker, M. Remškar and A. K. Hüttel, *Adv. Mater.*, 2023, **35**, 2209333.
18 S. Das, H.-Y. Chen, A. V. Penumatcha and J. Appenzeller, *Nano Lett.*, 2013, **13**, 100–105.
19 H. Choi, *et al.*, *ACS Nano*, 2019, **13**, 13169–13175.
20 R. Ławrowski, L. Pirker, K. Kaneko, H. Kokubo, M. Bachmann, T. Ikuno, M. Remškar and R. Schreiner, *J. Vac. Sci. Technol., B*, 2020, **38**, 032801.
21 D. R. Kazanov, *et al.*, *Appl. Phys. Lett.*, 2018, **113**, 101106.
22 I. A. Eliseyev, *et al.*, *Adv. Opt. Mater.*, 2023, **11**, 2202782.
23 M. Remškar, *et al.*, *Nanoscale Adv.*, 2024, **6**, 4075–4081.
24 R. T. K. Schock, *et al.*, *Phys. Status Solidi B*, 2024, **262**, 2400366.
25 C. Kim, *et al.*, *ACS Nano*, 2017, **11**, 1588–1596.
26 A. Di Bartolomeo, *et al.*, *2D Mater.*, 2018, **5**, 015014.
27 Y. Kim, T. Kim and E. K. Kim, *Nano Res.*, 2022, **15**, 6500–6506.
28 G. Vijayan, M. Uzhansky and E. Koren, *Appl. Phys. Lett.*, 2024, **124**, 13133101.
29 M. Ahmad, D. Varandani and B. R. Mehta, *Appl. Phys. Lett.*, 2018, **113**, 141603.
30 M. Cook, *et al.*, *Phys. Rev. B*, 2015, **92**, 201302.
31 K. Dolui, I. Rungger and S. Sanvito, *Phys. Rev. B: Condens. Matter Mater. Phys.*, 2013, **87**, 201302.
32 M. Precner, *et al.*, *Sci. Rep.*, 2018, **8**, 6724.
33 A. A. Koós, *et al.*, *Carbon*, 2016, **105**, 408–415.
34 Y. Li, Z. Zhou, S. Zhang and Z. Chen, *J. Am. Chem. Soc.*, 2008, **130**, 16739–16744.
35 A. Pezo, M. P. Lima, M. Costa and A. Fazzio, *Phys. Chem. Chem. Phys.*, 2019, **21**, 11359–11366.
36 H. Pan and Y.-W. Zhang, *J. Mater. Chem.*, 2012, **22**, 7280.
37 K. Wang, T. Taniguchi, K. Watanabe and J. Xue, *ACS Appl. Mater. Interfaces*, 2022, **14**, 39039–39045.
38 T.-X. Huang, *et al.*, *Nat. Commun.*, 2019, **10**, 20195544.
39 H. Qiu, T. Xu, Z. L. Wang, *et al.*, *Nat. Commun.*, 2013, **4**, 2642.
40 S. M. Hus and A.-P. Li, *Prog. Surf. Sci.*, 2017, **92**, 176–201.
41 G. Hao, *et al.*, *AIP Adv.*, 2013, **3**, 042125.
42 T. S. Jespersen and J. Nygård, *Nano Lett.*, 2005, **5**, 1838–1841.
43 B. C. Chapler, *et al.*, *Phys. Rev. B: Condens. Matter Mater. Phys.*, 2012, **86**, 165302.
44 W. Luo, *et al.*, *Nat. Commun.*, 2019, **10**, 2774.
45 F. Escudero, A. Sinner, Z. Zhan, P. A. Pantaleón and F. Guinea, *Phys. Rev. Res.*, 2024, **6**, 023203.
46 M. Kögl, P. Soubelet, M. Brotons-Gisbert, A. V. Stier, B. D. Gerardot and J. J. Finley, *npj 2D Mater. Appl.*, 2023, **7**, 32.
47 C. Moulsdale and V. Fal'ko, *Phys. Rev. B: Condens. Matter Mater. Phys.*, 2023, **107**, 144111.
48 M. J. Hamer, *et al.*, *ACS Nano*, 2022, **16**, 1954–1962.
49 M. Zhao, J. Zhuang, Q. Cheng, W. Hao and Y. Du, *Small*, 2019, **17**, 1903769.
50 J. Nathawat, *et al.*, *Nat. Commun.*, 2023, **14**, 1507.
51 D. Chen, *et al.*, *Nat. Commun.*, 2022, **13**, 4810.
52 A. Sinner, P. A. Pantaleón and F. Guinea, *Phys. Rev. Lett.*, 2023, **131**, 166402.
53 A. Ansh, U. Patbhaje, J. Kumar, A. Meersha and M. Shrivastava, *Commun. Mater.*, 2023, **4**, 8.
54 A. Ansh, J. Kumar, G. Sheoran and M. Shrivastava, *npj 2D Mater. Appl.*, 2020, **4**, 37.
55 W. Zhu, *et al.*, *Nat. Commun.*, 2014, **5**, 3087.
56 S. M. Gali, A. Pershin, A. Lherbier, J.-C. Charlier and D. Beljonne, *J. Phys. Chem. C*, 2020, **124**, 15076–15084.
57 R. Xu, *et al.*, *Nanotechnol*, 2018, **29**, 355701.
58 D. Oh, *et al.*, *Mater. Sci. Semicond. Process.*, 2023, **160**, 107424.
59 S. Sleziona, *et al.*, *Nanoscale Adv.*, 2023, **5**, 6958.
60 N. Kaushik, *et al.*, *npj 2D Mater. Appl.*, 2017, **1**, 34.
61 M. Chen, *et al.*, *ACS Nano*, 2014, **8**, 4023–4032.
62 J. Shu, *et al.*, *Nanoscale*, 2016, **8**, 3049.
63 J. Roh, J.-H. Lee, S. H. Jin and C. Lee, *J. Inf. Disp.*, 2016, **17**, 103–108.
64 D. Lee, J. Park, T. Kim, J. Lee and T. Kim, *ACS Appl. Nano Mater.*, 2025, **8**, 11185–11191.
65 J. Ludwig, *et al.*, *Nanotechnol*, 2019, **30**, 285705.